HAL
open science

U–Pb calcite dating reveals the origin of a 600 km-long intraplate fault: The Balcones Fault System of Texas

Jean-claude Hippolyte, Paul Mann, Pierre Henry, Abel Guihou, Pierre Deschamps, Camille Ourliac, Nicolas Godeau, Lionnel Marié, Mark B Gordon

HAL Id: hal-04666833
https://hal.inrae.fr/hal-04666833

Submitted on 2 Aug 2024

Terra Nova WILEY

RESEARCH ARTICLE

U–Pb calcite dating reveals the origin of a 600 km-long intraplate fault: The Balcones Fault System of Texas

Jean-Claude Hippolyte[1] | Paul Mann[2] | Pierre Henry[1] | Abel Guihou[1] | Pierre Deschamps[1] | Camille Ourliac[1] | Nicolas Godeau[1] | Lionnel Marié[1] | Mark B. Gordon[3]

[1]Aix Marseille Univ, CNRS, IRD, INRAE, CEREGE, Aix-en-Provence, France

[2]Department of Earth and Atmospheric Sciences, University of Houston, Houston, Texas, USA

[3]Independent, Cypress, Texas, USA

Correspondence
Jean-Claude Hippolyte, Aix Marseille Univ, CEREGE, Aix-en-Provence, BP80, 13545 CEDEX 04, France.
Email: hippolyte@cerege.fr

Abstract

Timing is a key data for understanding the origin of faulting. The Balcones fault system (BFS) extends ~600 km along the northern margin of the Gulf of Mexico oil basin and controls springs that supply the major cities in Texas, but its origin is unclear. We provide its first direct timing by applying U–Pb geochronology on seven calcite-mineralized fault surfaces. We have found that this extensional fault system formed during the Palaeocene-middle Eocene time (from 61.3 ± 2.7 to 45.4 ± 2.1 Ma), which is much earlier than previous estimates. We show that the formation of the BFS coincides with the largest clastic influx in the northern Gulf of Mexico basin that resulted from Laramide uplift and erosion. This timing and the location of the BFS along the Ouachita suture, support our interpretation of this fault system formed as the result of lithospheric flexure related to Paleogene sedimentary loading.

KEYWORDS
Balcones, fault, Geochronology, Gulf of Mexico, Laramide Orogeny, lithospheric flexure, Texas

1 | INTRODUCTION

When faulting occurs far from plate boundaries, its tectonic origin can be uncertain. Timing of faulting can be the key to discriminate between tectonic processes and other processes like raft salt tectonics, flexural response to sedimentary loading (e.g., Steinberg et al., 2014). U–Pb dating of calcite using the in-situ Laser Ablation Inductively Coupled Plasma-Mass Spectrometry (LA-ICP-MS) is being rapidly adopted by many groups for dating cements, veins and faults (e.g., Beaudoin et al., 2018; Godeau et al., 2018; Mottram et al., 2020; Parizot et al., 2020). Here, we apply U–Pb calcite geochronology to a large fault system to understand the origin of intraplate deformation.

The Balcones Fault System (BFS) is a ~40 km wide and ~600 km long, arcuate and extensional fault zone in central Texas to the north

of the Gulf of Mexico (GOM) basin (e.g., Ferrill & Morris, 2008; Figure 1). This normal fault system has uplifted by 350–500-m Lower Cretaceous limestone of the Edwards Plateau to the northwest relative to the Gulf Coastal Plain to the southeast (Ewing, 1991; Rose, 2016; Figure 2). The uplifted carbonates are intensely studied for their petroleum interest as part of the GOM series (e.g., Ewing & Galloway, 2019). However, the age of the BFS remains unclear, which impedes any credible tectonic interpretation. Extensional deformation appears unrelated to salt tectonics in the GOM because the normal faults lie northwest of the limit of the Louann salt layer (Figure 1). In order to understand its geodynamic origin, we apply U–Pb calcite geochronology on seven faults sampled from the BFS, and compare the absolute timing of fault slip with the long-term evolution of the northern GOM.

2 | GEOLOGICAL SETTING

The tectonic evolution of the northern GOM includes: (1) the opening of the GOM in the Late Triassic–Early Jurassic, (2) regional subsidence with deposition of the Louann evaporites in the late Middle Jurassic, (3) Jurassic sea-floor spreading, (4) carbonate shelf deposition on its passive margins during the Early and Middle Cretaceous and (5) latest Cretaceous to Eocene uplift and erosion during the Laramide orogeny (Ewing & Galloway, 2019; Filina et al., 2022; Rose, 2016; Worrall & Snelson, 1989).

During Cenozoic times, the northwestern margin of GOM Basin received a voluminous influx of siliciclastic sediments (Galloway & Williams, 1991). The clastic progradation displaced the shoreline and displaced the underlying salt (e.g., Diegel et al., 1995; Peel et al., 1995; Worrall & Snelson, 1989). The basinward rafting of the post-salt sedimentary column above the mobile Louann salt layer produced an updip breakaway zone or 'Peripheral Graben System' (Ewing, 2018; Figure 1).

The BFS forms a distinctive tectonic element lying west of the peripheral graben system and the Louann salt layer (Figure 1). Seismic and well data indicate that normal faults of the BFS penetrate Late Palaeozoic strata of the Ouachita fold belt (Ewing, 2005; Worrall & Snelson, 1989). Worrall and Snelson (1989) proposed that the basement-penetrating faults of the BFS formed as the result of extension related to the flexure and crustal downwarping of the northern GOM.

The age of formation for the BFS has been inferred by previous workers as starting ~23 Ma ago based on an erosional event of the Edwards Plateau inferred from the occurrence of Cretaceous limestone fragments in a matrix of Oligocene and Miocene sediments ~120 km southeast of the Balcones Fault Zone (Galloway, 2008; Rose, 2016; Weeks, 1945). However, the terrigenous clastic rocks of the Wilcox Group suggest that the Edwards carbonate platform section was already elevated above sea-level during the upper Palaeocene (Rose, 2016).

3 | METHODS

U–Pb dating of calcite can provide direct absolute dating of faulting provided that calcite precipitation can be reliably linked to fault slip (Roberts et al., 2020; Roberts & Holdsworth, 2022). To satisfy this requirement we only sampled striated fault surfaces. To ensure that the mineral growth being dated occurred during faulting, we performed structural analyses of polished thin sections normal to the fault plane and parallel to the striation. Cathodoluminescence (CL) microscopy was used to identify the compositional zoning and distinguish phases of calcite precipitation.

U–Pb analyses were carried out using an ESI 193nm laser ablation system coupled to an Element XR SF-ICP-MS following procedures adapted from Godeau et al. (2018). Calcite microstructures of potential different ages were analysed separately and directly

Significance Statement

We address the controls of intra-plate faulting that occurs far from an active plate boundary. We use U–Pb calcite geochronology to provide the first direct age dating of the ~600-km-long Balcones Fault System of Texas and we compare this timing with the long-term evolution of the northern Gulf of Mexico. We use five types of syn- and post- kinematic calcite structures for the U–Pb in-situ dating of fault slips. The Palaeocene–Eocene U–Pb age of the Balcones Fault System is much older than the Miocene age that has been assumed since the 1940s on the basis of stratigraphic data. We find that the timing of faulting coincides with the largest clastic influx in the northern Gulf of Mexico basin that was produced by the Laramide Orogeny and erosion in the Rocky Mountains. Intraplate faulting at Balcones records the onset of flexural response to the Cenozoic sedimentary loading along the northwestern margin of the Gulf of Mexico Basin. It is a far field consequence of the Laramide uplift and erosion.

on the studied 150 μm thick petrographic thin sections using Laser ablation spot size of 150 μm diameter. After data processing, ages for each selected calcite microstructures were derived from Tera–Wasserburg diagrams obtained using IsoplotR software (Vermeesch, 2018; Figures 3, 4 and 5; Data S1). WC1 was used as a primary standard to correct ^{238}U–^{206}Pb fractionation (Roberts et al., 2017) and AUG-B6 as a secondary standard (Pagel et al., 2018) to check for accuracy. Ages are quoted at 95% confidence interval including the propagation of systematic uncertainty of the standards following Horstwood et al. (2016). When the time of calcite precipitation was too long to give a single age, a Model Age method was used to estimate local laser spot ages by anchoring the isochron line to common lead value derived from concordant isochrons. The U/Pb dataset and more details on the methods are provided in the Data S1.

4 | RESULTS

We found unweathered calcite-filled fault surfaces at seven natural exposures along previously mapped strands of the BFS (Stoeser et al., 2005; Figure 2; Table 1; Data S2). All sampled normal faults strike northeast and exhibit dip-slip fault striations along fault planes (Figures 2, 4 and 5). This simple extensional tectonic setting allowed us to test the syn-kinematic reliability of various types of calcite structures found along fault surfaces, which include: (1) slickenfibres of stretching veins (Figures 3a and 4a) (e.g., Bons et al., 2012), (2) filled extensional jogs (Figure 5a,b) and (3) open vugs (e.g., Roberts

FIGURE 1 The Balcones Fault System, at the edge of the Gulf of Mexico basin. Bathymetry from the GEBCO Bathymetric Compilation Group 2019 (2019). Limit of Louann Salt deposits, lower Cretaceous Shelf Edge and Palaeozoic Ouachita Thrust front, from Ewing and Galloway (2019). Laramide structural front from Ferrill et al. (2019).
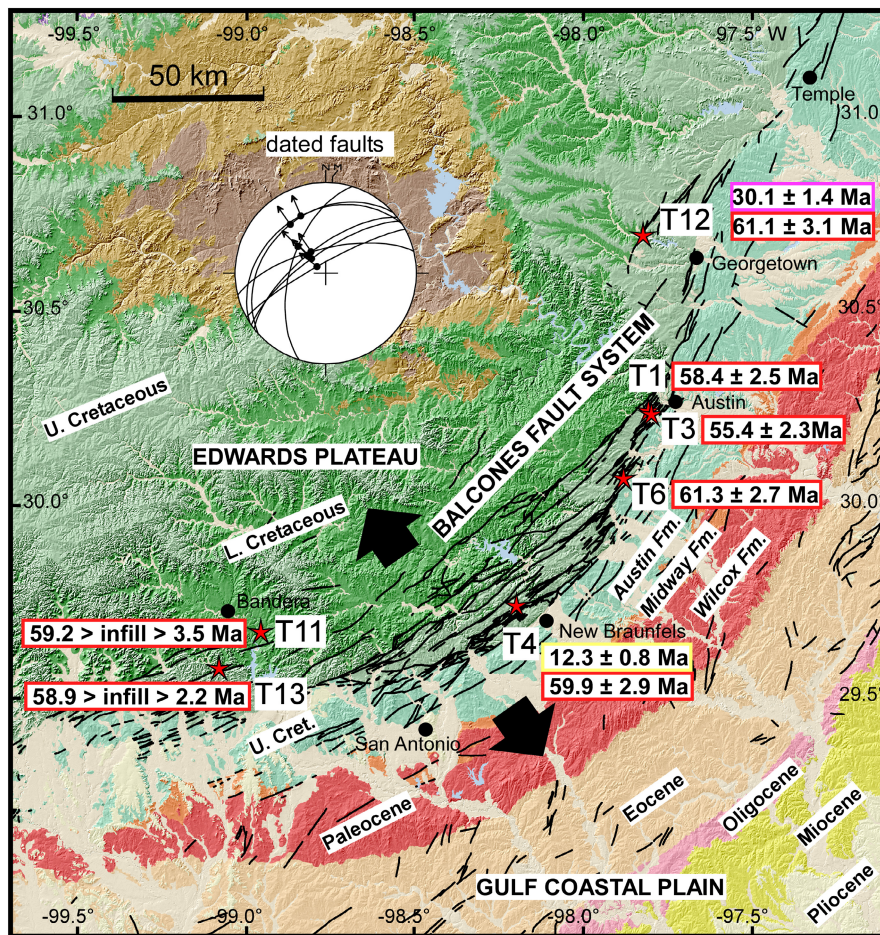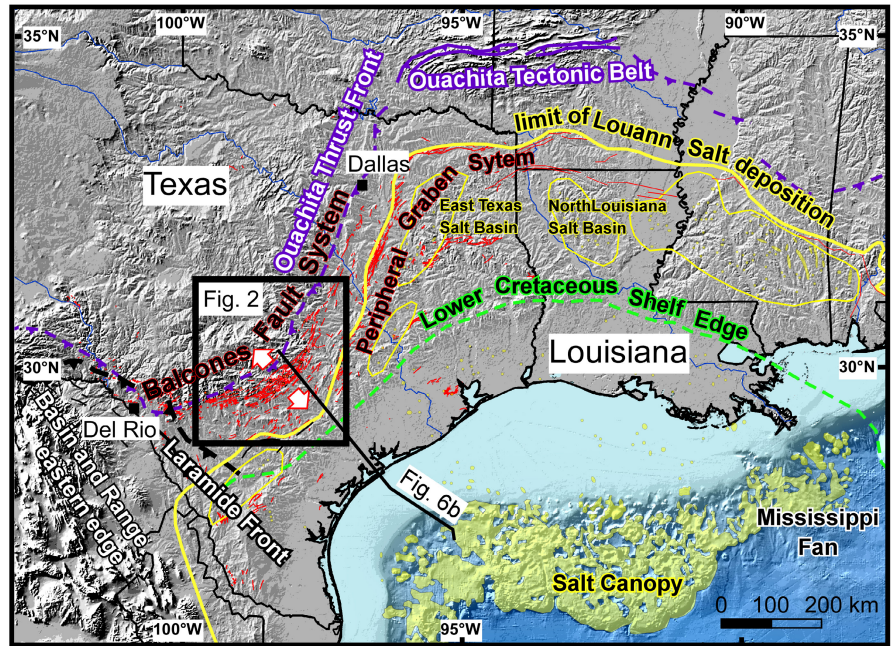

FIGURE 2 Shaded relief (Ryan et al., 2009) and the geological map of the Balcones Fault System (Stoeser et al., 2005) with Wilcox Group shown in red and Schmidt diagram and U–Pb ages of the sampled faults (Ma). The ages are quoted at the 95% confidence interval. The uncertainties include the propagation of systematic uncertainties of the standards.

& Holdsworth, 2022) (Figure 5c). Stretching veins, resulting from a crack-seal process, are the most reliably identifiable as syn-kinematic (Gaviglio, 1986; Roberts & Holdsworth, 2022).

Stretching veins with single-phase syn-kinematic calcite were found at sites T6 and T3 (Figure 3). Optical microscopy images showed characteristic features illustrated in Figures 3 and 4c. On T6 thin section, six areas of crack-seal sheared syn-kinematic calcite provided U–Pb intercept dates ranging from 61.3 ± 2.7 to 57.0 ± 2.5 Ma (Figure 3). Given that these dates of multiple crack-seal events cluster in a ca. 5 Ma long period during the Palaeocene, we propose a single period of normal faulting. On the T3 thin section, four areas of sheared syn-kinematic calcite of the crack-seal type provided dates ranging from 55.4 ± 2.4 to 45.4 ± 2.1 Ma. The age of the calcite youngs in the direction of shear and slickenfibres have episodically grown during ~10 Ma (Figure 3).

A stretching vein with two phases of syn-kinematic calcite was found at site T12 (Figures 2 and 4). Even though there is a unique trend of slickenfibres, CL microscopy revealed two different composition calcite infills (Figure 4c,d). Most of the vein is composed of dark luminescent calcite which includes: (1) crack-seal vein sequences, (2) calcite fibres and (3) blocky calcite. Younger light luminescent calcite is observed in three main settings: (1) along the shear-parallel veins, (2) in a pull-apart and healed microcracks connected to these shear veins and (3) and in the former center of the vein composed of thin calcite fibres coated by post-kinematic blocky calcite (Figure 4c, right side of the section). U–Pb dating confirms this relative chronology of calcite precipitation. Stage-1 calcite yielded a date of 61.1 ± 3.1 Ma. Stage-2 luminescent fibrous calcite in the pull-apart yielded a date of 29.8 ± 3.2 Ma (Figure 4d). Stage-2 luminescent blocky calcite yielded similar ages at three places (30.1 ± 1.4; 30.3 ± 1.4; 30.5 ± 1.5; Figure 4c). This blocky calcite coats the luminescent microcracks of stage-2 but precipitated shortly after fault slip (Figure 4c). Similar to fault T6, the main displacement on fault T12 occurred over multiple crack-seal events during the Palaeocene. The vein was overprinted during the Oligocene by a smaller fault slip (Figure 4d).

A single-phase extensional jog filled by unstretched blocky calcite was found along fault T1 (Figures 2 and 5a). Homogeneous and low-luminescent calcite suggests a single phase of fluid flow (Figure 5a). U–Pb measurements confirm a single age of calcite infill at 58.4 ± 2.5 Ma (Palaeocene). It is likely that calcite precipitation occurred shortly after fault slip and therefore as a consequence of the fault slip. For this reason, our calcite dates constrain the fault activity (Roberts & Holdsworth, 2022).

A multi-phase and filled extensional jog was observed on fault T4 (Figure 2). Stepped calcite slickenfibres are composed of three layers
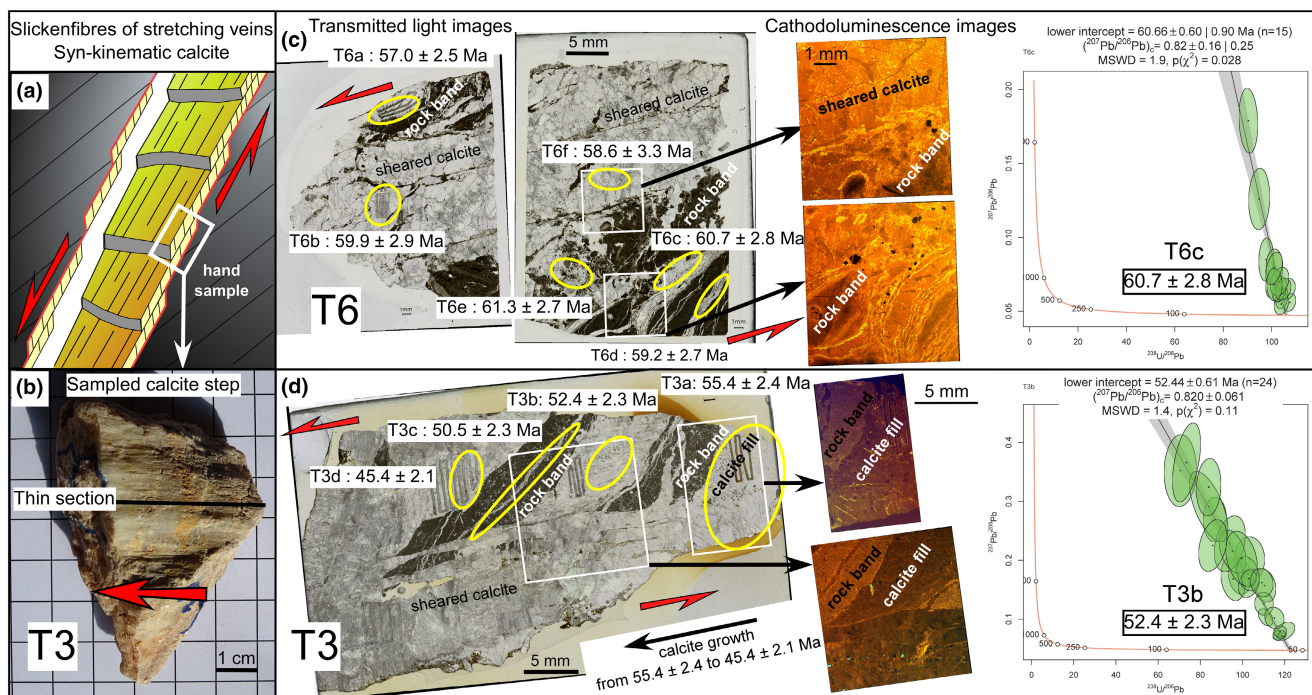

FIGURE 3 Stretching veins along faults T6 and T3. (a) Idealized stepped slickenfibres of stretching veins (overlapping stack of mineral filled extensional jogs). (b) Calcite step hand sample of fault T3. (c, d) Optical light and CL microscopy of thin sections cut parallel to the slickenlines. They show characteristic features formed by many incremental phases of crack-seal-slip mechanism (tiled sheets of sheared calcite, alternating calcite veins and host rock lithons). U–Pb age data are shown on Tera–Wasserburg diagrams here and in Data S2 (error ellipse = 2s). IsolpotR Tera–Wasserburg diagrams of the LASER ablation spot analyses (Vermeesch, 2018), with the age $\pm 1s$ |2s |2s corrected for overdispersion, n = number of spot analyses, initial $^{207}Pb/^{206}Pb$ and MSWD (mean squared weighted deviations). The uncertainties provided include the propagation of systematic uncertainty of the standards. Calcite infill is syn-kinematic and the dated mineral growth dates the fault slips. T3 calcite step has grown during ~10 Ma.
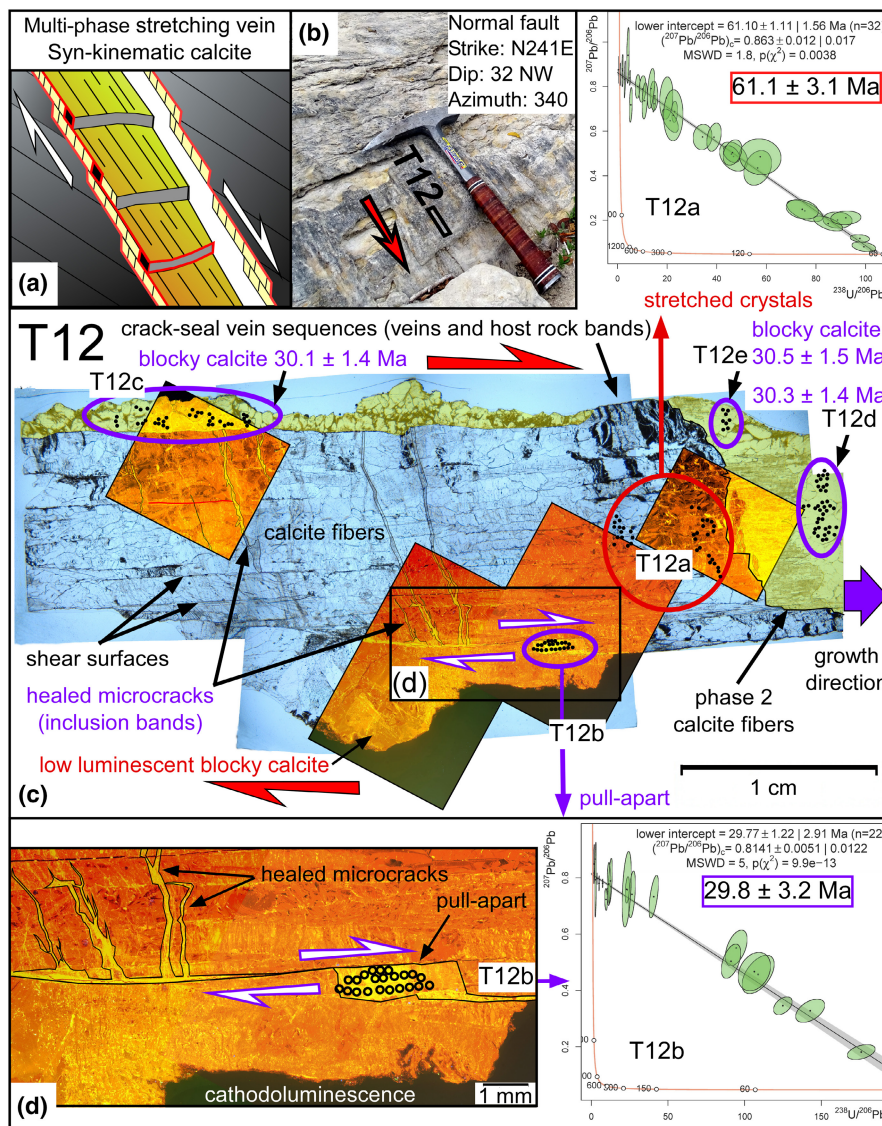
FIGURE 4 Stretching vein along fault T12 showing two phases of syn-kinematic calcite infill. (a) Idealized stepped slickenfibres. (b) Sampled fault surface. (c) Optical microscopy images with characteristic crack-seal mineral fill features. Light colours on CL images show a pull-apart and microcracks filled by a younger phase of syn-kinematic calcite precipitation (d). Black dots and circles show laser beam ablation spots. U–Pb age data are shown on Tera–Wasserburg diagrams.

of alternatively low and high luminescent and elongated blocky calcite (Figure 5b). The U–Pb age of each layer is younger toward the center of the vein: 59.9 ± 2.9; 57.1 ± 3.4 and 12.3 ± 0.8 Ma. In contrast with the stretching veins, syntaxial growth of calcite occurred through three phases opening along the vein center with each phase marked by distinctive fluid precipitations. Two intervals of calcite precipitation following fault slip occurred during the Palaeocene and one during the Middle Miocene.

Post-kinematic euhedral calcite crystals in open vugs were observed on faults T11 and T13 (Figures 2 and 5c). CL microscopy revealed colour zoning parallel to the crystal faces. U–Pb dating does not provide a single age for this colour zonation. The initial $^{207}Pb/^{206}Pb$ ratio derived from the Tera–Wasserburg isochron of sample T13 (i.e., $^{207}Pb/^{206}Pb = 0.83$) was used to anchor the model age for each individual measurement spots for T11 and T13. Spot dates range from ca. 59 to 3 Ma for T11 and from ca. 59 to 2 Ma for T13, with younger ages

in the outer crystal zones (Figure 5c). Calcite has not fully filled the jog and cannot provide a unique date, but the oldest dates of calcite precipitation constrain the age of fault slip and fractures opening. The Palaeocene dates along faults T11 and T13 are consistent with the Palaeocene age of BFS faulting at T1, T4, T6 and T12 (Figure 6).

5 | DISCUSSION

Sixteen ages from the seven sites along the BFS cluster in the Palaeocene–Eocene (ca. 61–45 Ma). Although calcite ages may not capture the complete history of fault displacement, this timing of BFS faulting is clearly: (1) much younger than its Early Cretaceous carbonate host rock (>100 Ma; Figure 6) and (2) much older than the previous Oligocene-Miocene estimate (Weeks, 1945).
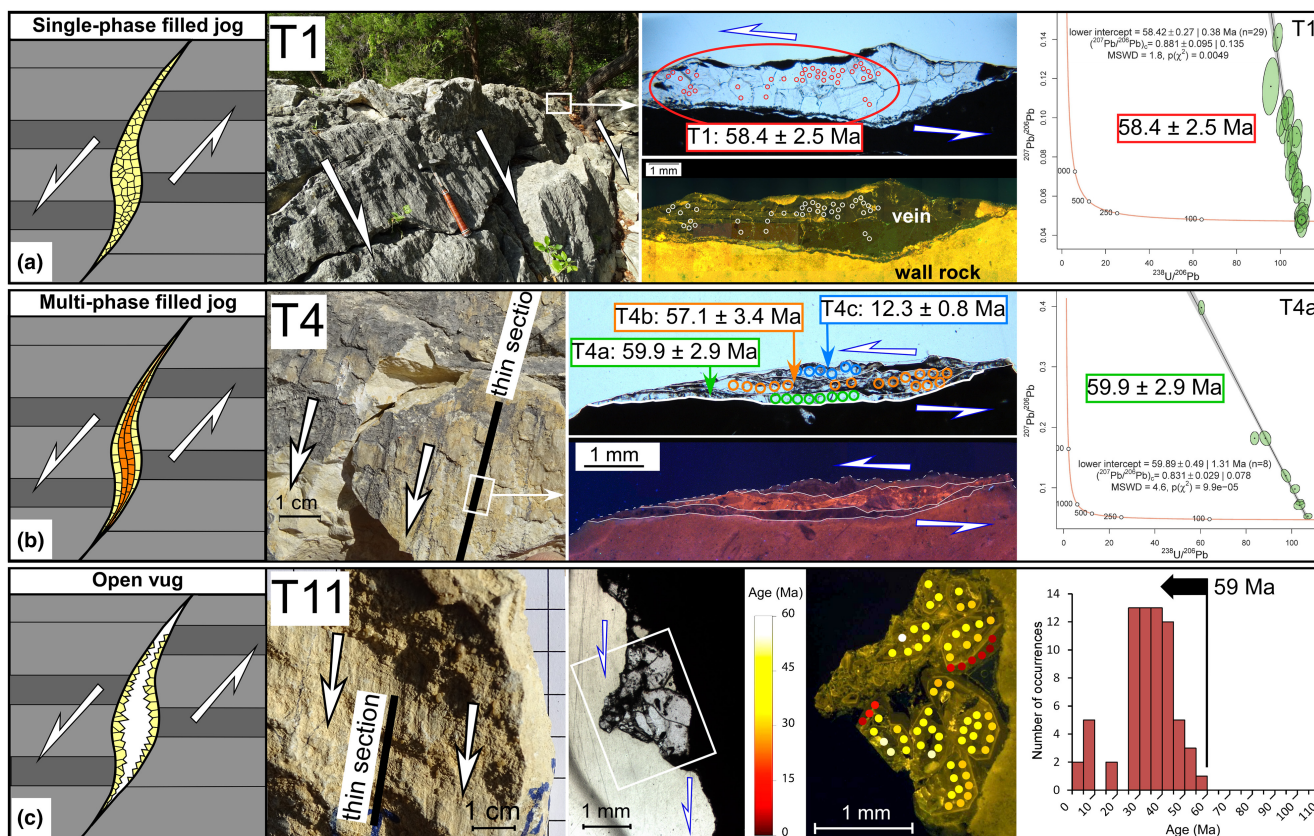
FIGURE 5 Three types of calcite infill at extensional fault jogs observed along striated normal faults (modified from Roberts & Holdsworth, 2022): (a) single-phase filled jog, (b) multi-phase filled jog, (c) open vug. For each type we show an outcrop view, transmitted light and CL images of thin sections and U–Pb age diagrams. For (c) dots and histogram show the distribution of individual ages.

This timing is coincident with the first major clastic influx in the northern GOM recorded by the up to 3-km-thick Palaeocene–Eocene Wilcox Group that marks a major shift from a carbonate shelf-ramp system to a siliciclastic wedge (e.g., Mackey et al., 2012; Sharman et al., 2017). Using thickness maps, Galloway et al. (2011) calculated the rate of sediment supply in the northern GOM Basin through time. After a ~3 Ma phase of sediment starvation (Midway Formation), supply increased abruptly in the Late Palaeocene with deposition of the Lower Wilcox prograding fluvial-deltaic sequence that reached the highest grain volume rate, exceeding $150,000 \, km^3/$ Ma (Figure 6). This pulse of sediment delivery also coincided with major progradation of the shoreline. Wilcox sediment was mainly derived from Laramide uplifts of the southern Rocky Mountains, northern Mexico and the Cordilleran magmatic arc and most authors emphasize the importance of drainage systems reorganization and Laramide orogeny for the Palaeocene increase and Eocene decrease in sediment supply (Ewing & Galloway, 2019; Galloway et al., 2011; Mackey et al., 2012; Sharman et al., 2017; Snedden et al., 2018; Wahl et al., 2016).

The Laramide orogeny reached southern New Mexico in the Late Campanian (75 ± 1.1 Ma) (Amato et al., 2017; Jones et al., 2011) and western Texas at ~70 Ma (Lehman, 1991). Deformation had ceased in New Mexico prior to the final episode of Laramide magmatism starting at ~46 Ma (Amato et al., 2017) and continued north of Texas until 40–35 Ma (Bird, 1998) or 28 Ma (Beaudoin et al., 2018). Thereby, our ages for the BFS show that the fault zone formed when the Laramide Mountain building was active to the West (Figure 6). Note that the Laramide contraction had not reached the BFS area and that a far field effect of this contraction would not explain the Oligocene and Miocene reactivations of the BFS (Figures 4, 5 and 6).

Previous authors suggested that the BFS formed during crustal flexure related to sediment loading in the downdip area of the GOM (Rose, 2016; Worrall & Snelson, 1989). The coincidence of the three dated BFS periods of fault slip with the three main sedimentary pulses in the GOM (Palaeocene, Oligocene and Middle Miocene) supports a flexure model with bending stresses activating episodically the BFS (Figure 6). Structural maps and cross sections show that the BFS overlies a zone of pre-existing weakness, the Palaeozoic Ouachita suture separating thick Proterozoic crust and the thinner GOM crust (Ewing, 2005; Ewing & Galloway, 2019; Rose, 2016; Worrall & Snelson, 1989; Figures 1 and 6). This superposition supports the idea that lithospheric flexure of the northern GOM margin has locally reactivated the Ouachita zone of crustal weakness.

TABLE 1 Structural setting and dates of the analysed calcite samples.

Site name	Latitude (°N)	Longitude (°W)	Rock formation	Normal fault striation Strike	Dip	Rake	Azimuth	Calcite structure	Calcite fill kinematics	Number of data-points	$^{207}Pb/^{206}Pb$	Age (Ma)	2s (corrected for overdispersion if $p(\chi^2)<0.05$)	2s (systematic uncertainties propagated)	MSWD	$p(\chi^2)$	Stratigraphic age
T1	30.24900	97.81285	Edwards Limestone	228	67NW	−87		Blocky elongated	Syn-kinematic	29	0.88±0.13	58.42	0.38	2.54	1.80	<0.05	Palaeocene (Selandian-Thanetian)
T3a	30.24406	97.81055	Edwards Limestone	224	34NW		140	Blocky streched	Syn-kinematic	30	0.80±0.10	55.43	0.48	2.44	3.10	<0.05	Palaeocene-Eocene
T3b								Blocky streched	Syn-kinematic	24	0.82±0.06	52.40	0.60	2.34	1.40	0.11	Eocene (Ypresian)
T3c								Blocky elongated	Syn-kinematic	30	0.69±0.03	50.54	0.72	2.29	3.60	<0.05	Eocene (Ypresian)
T3d								Blocky streched	Syn-kinematic	22	0.82±0.04	45.42	0.78	2.11	2.50	<0.05	Eocene (Lutetian)
T4a	29.74491	98.20379	Edwards Limestone	193	58W	−105		Blocky elongated	Syn-kinematic	8	0.83±0.08	59.89	1.31	2.89	4.60	<0.05	Palaeocene
T4b								Blocky elongated	Syn-kinematic	16	0.83±0.02	57.09	2.37	3.42	12.00	<0.05	Palaeocene-Eocene
T4c								Blocky elongated	Syn-kinematic	6	0.83±0.02	12.29	0.64	0.83	3.80	<0.05	Serravallian
T6a	30.06818	97.87729	Edwards Limestone	231	72NW	−87		Blocky streched	Syn-kinematic	30	0.84±0.01	57.02	0.41	2.49	2.40	<0.05	Palaeocene-Eocene
T6b								Blocky streched	Syn-kinematic	22	0.81±0.07	59.85	1.36	2.91	4.10	<0.05	Palaeocene
T6c								Blocky streched	Syn-kinematic	15	0.82±0.25	60.66	0.90	2.76	1.90	<0.05	Palaeocene
T6d								Blocky streched	Syn-kinematic	19	0.68±0.1	59.17	0.78	2.67	2.50	<0.05	Palaeocene
T6e								Blocky streched	Syn-kinematic	19	0.82±0.02	61.28	0.38	2.67	1.60	0.06	Palaeocene
T6f								Blocky streched	Syn-kinematic	17	0.82±0.02	58.59	2.15	3.32	2.10	<0.05	Palaeocene-Eocene
T12a	30.69637	97.82835	Edwards Limestone	241	32NW		340	Fibrous streched	Syn-kinematic	32	0.86±0.02	61.10	1.56	3.06	1.80	<0.05	Palaeocene
T12b								Fibrous streched	Syn-kinematic	22	0.81±0.01	29.77	2.91	3.18	5.00	<0.05	Oligocene
T12c								Blocky	Post-kinematic	36	0.79±0.02	30.05	0.50	1.39	4.50	<0.05	Oligocene
T12d								Blocky	Post-kinematic	38	0.87±0.04	30.32	0.46	1.38	1.70	<0.05	Oligocene
T12e								Blocky	Post-kinematic	8	0.85±0.05	30.49	0.67	1.47	0.77	0.59	Oligocene
T11	29.67359	98.96028	Glen Rose Limestone	252	68NW	−82		Blocky	Post-kinematic	69	0.83	≤59.2±10Ma					From Palaeocene to Pliocene
T13	29.57837	99.08423	Glen Rose Limestone	237	81NW	−86		Blocky	Post-kinematic	152	0.83	≤58.9±4Ma					From Palaeocene to Quaternary

Note: Geographic coordinates of the sampled striated fault surfaces, name of the host rock formation, fault attitude and striation, type of calcite texture and kinematic interpretation from thin section analyses, number of laser spot analyses, $^{207}Pb/^{206}Pb$, U–Pb dates, 2s uncertainties, 2s uncertainties with propagation of systematic uncertainties (Horstwood et al., 2016), MSWD parameter (Mean Square of Weighted Deviation), $p(\chi^2)$, Stratigraphic age.
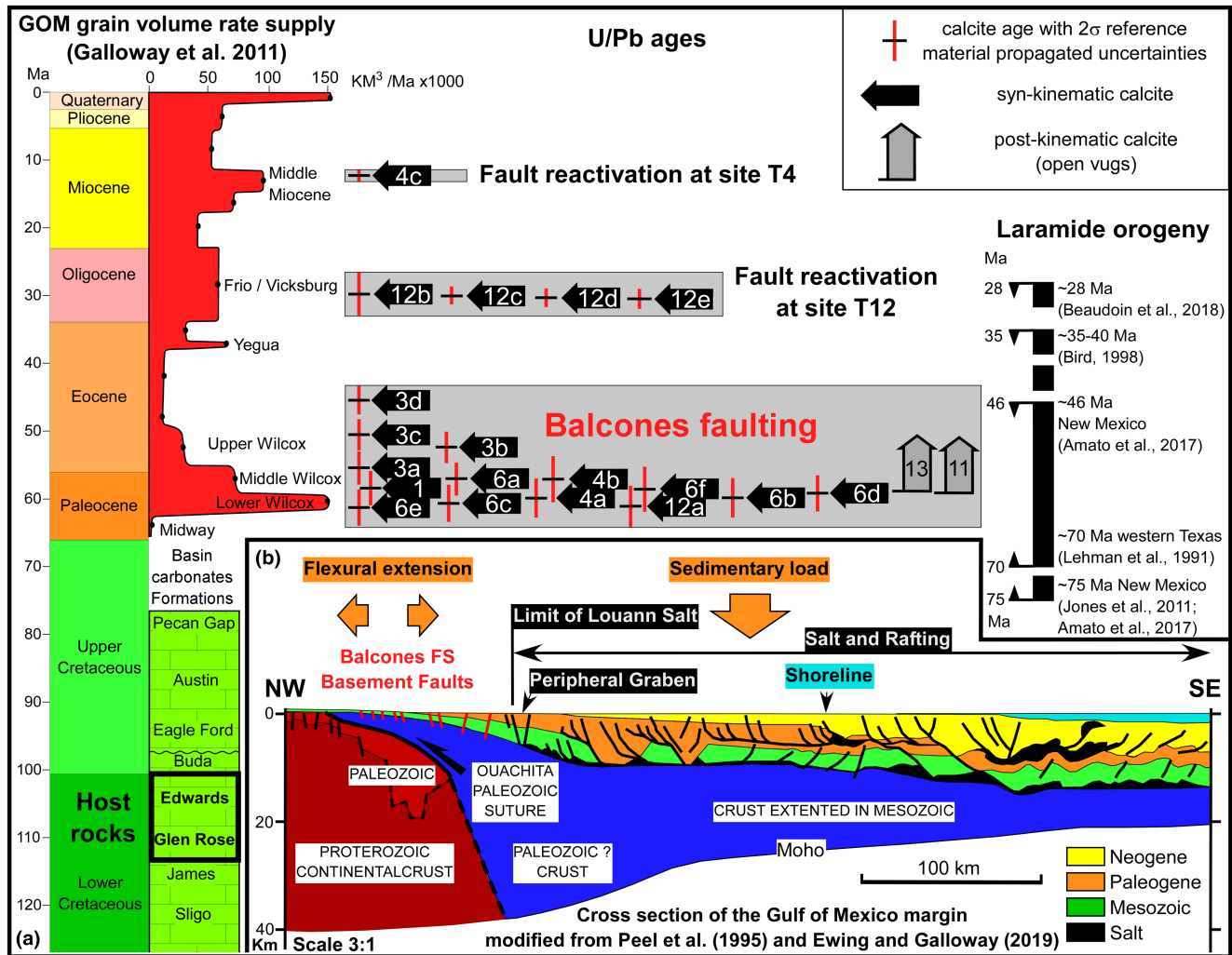
FIGURE 6 (a) Stratigraphic scale showing the host rocks, variations in the relative rate of clastic supply in the northern GOM basin, U–Pb dates of fault slip and age range for the Laramide orogenic event. (b) Structural transect of the GOM margin with location of the BFS and the Palaeogene Wilcox Group (location on Figure 1).

6 | CONCLUSIONS

This study demonstrates the syn-kinematic reliability of five types of calcite structures for U–Pb in-situ dating when combined with microstructural and CL analyses. It provides the first absolute timing on the fault motions along the BFS.

The Palaeocene-middle Eocene timing of BFS faulting is coincident with the largest clastic influx on the GOM margin (Wilcox Group) resulting from Laramide uplift and its related increase in size of fluvial drainage basins.

We propose that BFS extensional faulting occurred as the result of bending stresses and basement reactivation along the Ouachita suture during Paleogene sedimentary loading and lithospheric flexure of the northern GOM margin. This flexural model explains the location of the BFS along the reactivated Ouachita suture at the transition between thick and thin crust and outside the raft tectonics area.

Absolute timing places the BFS as a forerunner of the Gulf of Mexico Neogene gravity driven tectonics. Its Oligocene and Miocene local reactivations also support the conclusion that faults slips occurred during clastic influxes.

ORCID

Jean-Claude Hippolyte https://orcid.org/0000-0003-0812-8992

REFERENCES

Amato, J. M., Mack, G. H., Jonell, T. N., Seager, W. R., & Upchurch, G. R. (2017). Onset of the Laramide orogeny and associated magmatism in southern New Mexico based on U–Pb geochronology. *GSA Bulletin, 129*, 1209–1226. https://doi.org/10.1130/B31629.1

Beaudoin, N., Lacombe, O., Roberts, N. M. W., & Koehn, D. (2018). U–Pb dating of calcite veins reveals complex stress evolution and thrust

sequence in the Bighorn Basin, Wyoming, USA. *Geology, 46,* 1015–1018. https://doi.org/10.1130/G45379.1

Bird, P. (1998). Kinematic history of the Laramide orogeny in latitudes 35 degrees–49 degrees N, western United States. *Tectonics, 17,* 780–801. https://doi.org/10.1029/98TC02698

Bons, P., Elburg, M., & Gomez-Rivas, E. (2012). A review of the formation of tectonic veins and their microstructures. *Journal of Structural Geology, 43,* 33–62. https://doi.org/10.1016/j.jsg.2012.07.005

Diegel, F. A., Karlo, J. F., Schuster, D. C., Shoup, R. C., & Tauvers, P. R. (1995). Cenozoic structural evolution and tectono-stratigraphic framework of the northern Gulf Coast continental margin. In M. P. A. Jackson, D. G. Roberts, & S. Snelson (Eds.), *Salt tectonics: A global perspective* (Vol. *65,* pp. 109–151). AAPG Memoir.

Ewing, T. E. (1991). *The tectonic framework of Texas: Text to accompany "The Tectonic Map of Texas"* (p. 36). Texas Bureau of Economic Geology.

Ewing, T. E. (2005). *Phanerozoic development of the Llano uplift* (pp. 15–25). South Texas Geological Society Bulletin.

Ewing, T. E. (2018). The peripheral graben system in Texas: An overview. *Gulf Coast Association of Geological Societies Transactions, 68,* 163–178.

Ewing, T. E., & Galloway, W. E. (2019). Evolution of the northern Gulf of Mexico Sedimentary Basin. In A. D. Miall (Ed.), *The sedimentary basins of the United States and Canada* (pp. 627–694). Elsevier. https://doi.org/10.1016/B978-0-444-63895-3.00016-4

Ferrill, D. A., & Morris, A. P. (2008). Fault zone deformation controlled by carbonate mechanical stratigraphy, Balcones fault system, Texas. *AAPG Bulletin, 92,* 359–380.

Ferrill, D. A., Morris, A. P., & McGinnis, R. N. (2019). Geologic structure of the Edwards (Balcones Fault Zone) aquifer. In J. M. Sharp, Jr., R. T. Green, & G. M. Schindel (Eds.), *The Edwards aquifer: The past, present, and future of a vital water resource* (Vol. *215,* pp. 171–188). Geological Society of America Memoirs. https://doi.org/10.1130/2019.1215(14)

Filina, I., Austin, J., Doré, T., Johnson, E., Minguez, D., Norton, I., Snedden, J., & Stern, R. J. (2022). Opening of the Gulf of Mexico: What we know, what questions remain, and how we might answer them. *Tectonophysics, 822*(229), 150. https://doi.org/10.1016/j.tecto.2021.229150

Galloway, W. E. (2008). Depositional evolution of the Gulf of Mexico Sedimentary Basin. In A. D. Miall (Ed.), *The sedimentary basins of the United States and Canada* (pp. 505–549). Elsevier. https://doi.org/10.1016/S1874-5997(08)00015-4

Galloway, W. E., Whiteaker, T. L., & Ganey-Curry, P. (2011). History of Cenozoic North American drainage basin evolution, sediment yield, and accumulation in the Gulf of Mexico basin. *Geosphere, 7,* 938–973. https://doi.org/10.1130/GES00647.1

Galloway, W. E., & Williams, T. A. (1991). Sediment accumulation rates in time and space: Paleogene genetic stratigraphic sequences of the northwestern Gulf of Mexico basin. *Geology, 19,* 986–989. https://doi.org/10.1130/0091-7613(1991)019<0986:SARITA>2.3.CO;2

Gaviglio, P. (1986). Crack-seal mechanism in a limestone: A factor of deformation in strike-slip faulting. *Tectonophysics, 131,* 247–255.

GEBCO Bathymetric Compilation Group 2019. (2019). *The GEBCO_2019 Grid—A continuous terrain model of the global oceans and land.* British Oceanographic Data Centre, National Oceanography Centre, NERC. https://doi.org/10.5285/836f016a-33be-6ddc-e053-6c86abc0788e

Godeau, N., Deschamps, P., Guihou, A., Leonide, P., Tendil, A., Gerdes, A., Hamelin, B., & Girard, J.-P. (2018). U–Pb dating of calcite cement and diagenetic history in microporous carbonate reservoirs: Case of the Urgonian limestone, France. *Geology, 46,* 247–250. https://doi.org/10.1130/G39905.1

Horstwood, M. S. A., Košler, J., Gehrels, G., Jackson, S. E., McLean, N. M., Paton, C., Pearson, N. J., Sylvester, P., Vermeesch, P., Bowring, J. F., Condon, D., & Schoene, B. (2016). Community-derived standards for LA-ICP-MS U-(Th-) Pb geochronology-uncertainty propagation, age interpretation and data reporting. *Geostandards and Geoanalytical Research, 40,* 311–332.

Jones, C. H., Farmer, G. L., Sageman, C., & Zhong, S. (2011). Hydrodynamic mechanism for the Laramide orogeny. *Geosphere, 7,* 183–201. https://doi.org/10.1130/GES00575.1

Lehman, T. M. (1991). Sedimentation and tectonism in the Laramide Tornillo Basin of West Texas. *Sedimentary Geology, 75,* 9–28.

Mackey, G. N., Horton, B. K., & Milliken, K. L. (2012). Provenance of the Paleocene-Eocene Wilcox Group, western Gulf of Mexico basin: Evidence for integrated drainage of the southern Laramide Rocky Mountains and Cordilleran arc. *Geological Society of America Bulletin, 124,* 1007–1024. https://doi.org/10.1130/B30458.1

Mottram, C. M., Kellett, D. A., Barresi, T., Zwingmann, H., Friend, M., Todd, A., & Percival, J. B. (2020). Syncing fault rock clocks: Direct comparison of U–Pb carbonate and K–Ar illite fault dating methods. *Geology, 48,* 1179–1183. https://doi.org/10.1130/G47778.1

Pagel, M., Bonifacie, M., Schneider, D. A., Gautheron, C., Brigaud, B., Calmels, D., Cros, A., Saint-Bezar, B., Landrein, P., Sutcliffe, C., Davis, D., & Chaduteau, C. (2018). Improving paleohydrological and diagenetic reconstructions in calcite veins and breccia of a sedimentary basin by combining $\Delta 47$ temperature, $\delta 18Owater$ and U–Pb age. *Chemical Geology, 481,* 1–17.

Parizot, O., Missenard, Y., Vergely, P., Haurine, F., Noret, A., Delpech, G., Barbarand, J., & Sarda, P. (2020). Tectonic record of deformation in intraplate domains: Case study of far-field deformation in the grands causses area, France. *Geofluids, 2020,* 7598137. https://doi.org/10.1155/2020/7598137

Peel, F. J., Travis, C. J., & Hossack, J. R. (1995). Genetic structural provinces and salt tectonics of the Cenozoic offshore U.S. Gulf of Mexico, a preliminary analysis. In M. P. A. Jackson, D. G. Roberts, & S. Snelson (Eds.), *Salt tectonics: A global perspective* (Vol. *65,* pp. 153–176). AAPG Memoir.

Roberts, N. M. W., Drost, K., Horstwood, M. S., Condon, D. J., Chew, D., Drake, H., Milodowski, A. E., McLean, N. M., Smye, A. J., Walker, R. J., & Haslam, R. (2020). Laser ablation inductively coupled plasma mass spectrometry (LA-ICP-MS) U–Pb carbonate geochronology: Strategies, progress, and limitations. *Geochronology, 2,* 33–61.

Roberts, N. M. W., & Holdsworth, R. E. (2022). Timescales of faulting through calcite geochronology: A review. *Journal of Structural Geology, 158*(104), 578. https://doi.org/10.1016/j.jsg.2022.104578

Roberts, N. M. W., Rasbury, E. T., Parrish, R. R., Smith, C. J., Horstwood, M. S. A., & Condon, D. J. (2017). A calcite reference material for LA-ICP-MS U–Pb geochronology. *Geochemistry, Geophysics, Geosystems, 18,* 2807–2814.

Rose, P. R. (2016). Late cretaceous and tertiary burial history, Central Texas. *GCAGS Journal, 5,* 141–179.

Ryan, W. B. F., Carbotte, S. M., Coplan, J., O'Hara, S., Melkonian, A., Arko, R., Weissel, R. A., Ferrini, V., Goodwillie, A., Nitsche, F., Bonczkowski, J., & Zemsky, R. (2009). Global multi-resolution topography (GMRT) synthesis data set. *Geochemistry, Geophysics, Geosystems, 10,* Q03014. https://doi.org/10.1029/2008GC002332

Sharman, G. R., Covault, J. A., Stockli, D. F., Wroblewski, A. F. J., & Bush, M. A. (2017). Early Cenozoic drainage reorganization of the United States Western Interior-Gulf of Mexico sediment routing system. *Geology, 45*(2), 187–190. https://doi.org/10.1130/G38765.1

Snedden, J. W., Tinker, L. D., & Virdell, J. (2018). Southern Gulf of Mexico Wilcox source to sink: Investigating and predicting Paleogene Wilcox reservoirs in eastern Mexico deep-water areas. *AAPG Bulletin, 102*(10), 2045–2074.

Steinberg, J., Gvirtzman, Z., & Garfunkel, Z. (2014). Flexural response of a continental margin to sedimentary loading and lithospheric rupturing: The mountain ridge between the Levant Basin and the Dead

Sea transform. *Tectonics*, *33*, 166–186. https://doi.org/10.1002/2013TC003330

Stoeser, D. B., Shock, N., Green, G. N., Dumonceaux, G. M., & Heran, W. D. (2005). *Geologic map database of Texas*. U.S. Geological Survey, DS 170, scale 1:500,000.

Vermeesch, P. (2018). IsoplotR: A free and open toolbox for geochronology. *Geoscience Frontiers*, *9*, 1479–1493. https://doi.org/10.1016/j.gsf.2018.04.001

Wahl, P. J., Yancey, T. E., Pope, M. C., Miller, B. V., & Ayers, W. B. (2016). U–Pb detrital zircon geochronology of the Upper Paleocene to Lower Eocene Wilcox Group, east-central Texas. *Geosphere*, *12*, 1517–1531. https://doi.org/10.1130/GES01313.1

Weeks, A. W. (1945). Balcones, Luling and Mexia fault zones in Texas. *AAPG Bulletin*, *29*, 1733–1737.

Worrall, D. M., & Snelson, S. (1989). Evolution of the northern Gulf of Mexico, with emphasis on Cenozoic growth faulting and the role of salt. In A. W. Bally & A. R. Palmer (Eds.), *The geology of North America—An overview* (pp. 97–137). Geological Society of America.

SUPPORTING INFORMATION

Additional supporting information can be found online in the Supporting Information section at the end of this article.

Data S1.

Data S2.

How to cite this article: Hippolyte, J.-C., Mann, P., Henry, P., Guihou, A., Deschamps, P., Ourliac, C., Godeau, N., Marié, L., & Gordon, M. B. (2024). U–Pb calcite dating reveals the origin of a 600 km-long intraplate fault: The Balcones Fault System of Texas. *Terra Nova*, *00*, 1–10. https://doi.org/10.1111/ter.12734